Journal of Materials Research and Technology 27 (2023) 8008–8022

Contents lists available at ScienceDirect

Journal of Materials Research and Technology

journal homepage: www.elsevier.com/locate/jmrt

Microstructure and mechanical performance of low-cost biomedical-grade Titanium-316L alloy

Chowdhury Ahmed Shahed [a], Faiz Ahmad [a,*], Ebru Günister [b], Khurram Altaf [a], Saad Ali [a], Abbas Raza [a], Khurshid Malik [a], Waseem Haider [c]

[a] Department of Mechanical Engineering, University Teknologi PETRONAS, Persiaran UTP, 32610, Seri Iskandar, Perak, Malaysia
[b] Faculty of Engineering and Natural Sciences, Department of Mechanical Engineering, Istanbul Health and Technology University, 34275, Istanbul, Turkey
[c] School of Engineering and Technology, Central Michigan University, 1200 S Franklin St, Mt Pleasant, MI, 48859, United States

ARTICLE INFO

Keywords:
Biomedical implants
Beta titanium
Powder injection molding
Transgranular crack
Wear resistance
316L stainless steel

ABSTRACT

A 316L stainless steel (SS) alloy was developed with 1, 3, and 5 vol% titanium (Ti) reinforcement using the powder injection molding route, representing a low-cost option for biomedical implants. The investigation encompassed 1300 °C, 1350 °C, and 1380 °C sintering temperatures to ascertain the optimal physical and mechanical properties. Both sintering temperature and Ti influenced sintered density, and Ti mitigated the deleterious effects of residual carbon. At higher sintering temperatures, carbon and silicon tended to migrate and accumulate at the brink of Ti, leading to the formation of intermetallic compounds and increased brittleness. Dispersed Ti particles within the 316L matrix acted as nucleation sites and enhanced solid solubility with improved density. An astounding 96.11 % sintered density was achieved at 3 vol% Ti sample sintered at 1380 °C. During the tensile test, 5 vol% Ti at 1380 °C exhibited a low modulus of 58.9 GPa, which is highly desirable for orthopedic implant application. The XRD, SEM, tensile test, and nano-indentation results collectively provide evidence of beta-titanium formation during the sintering process. Conversely, the sample incorporating 3 vol% titanium, sintered at 1380 °C, demonstrated a balanced performance, showcasing 432.94 ± 12.8 MPa ultimate tensile strength, 3.06 ± 0.17 % elongation, 74.2 GPa modulus, and 322 MPa and 423 MPa 0.2 % offset flexural and compressive yield strengths, respectively. Notably, an improvised wear resistance test underscored its aptitude for sliding wear resistance, solidifying its potential as a promising candidate for biomedical implants.

1. Introduction

Owing to the ability to produce complex shapes and customized designs, additive manufacturing (AM) is used extensively in fabricating metal components. But, the relatively slow production throughput, high production cost, undesired surface roughness, and post-production surface finishing make AM less feasible for mass-producing biomedical parts [1,2]. The layer-by-layer build technique often introduces layer separation during tension and deteriorates the mechanical strength [3]. Therefore, PIM is still irreplaceable for its straightforward, relatively faster, low-cost, net or near-net shape fabrication techniques and complex geometric part production capabilities [4]. It requires different polymer binders to mix with main powders to produce feedstock for injection. These residual binders are a significant carbon source in the sintered part, increasing corrosion susceptibility, brittleness, and high elastic modulus, which is detrimental, especially for biomedical implants [5]. Hence, proper material selection must be considered to neutralize such effects by absorbing carbon in their matrix.

Ti and its alloys are famous for their biocompatibility, excellent mechanical properties, and corrosion resistance abilities [6,7]. The modulus of pure Ti is 120 GPa [8], and it is further going down to 40–80 GPa for beta titanium (β-Ti) alloys [9], thus making it a great promising material for orthopedic implants. Ti itself and the commonly used non-toxic β stabilizing elements, such as niobium (Nb) and tantalum (Ta), make the implant highly expensive [10]. Contrarily, SS is relatively economical, and a 300-series austenitic SS is also renowned for its corrosion resistance, high strength-to-weight ratio, non-magnetic behavior, ductility, and toughness [11]. Being a low-carbon variant in the 300-series with high nickel and Mo content, 316L SS exhibits improved acid resistance, especially pitting and crevice corrosion in chloride environments, and chromium (Cr) is responsible mainly for giving protection against corrosion [12]. Despite that, due to the body

* Corresponding author.
E-mail address: faizahmad@utp.edu.my (F. Ahmad).

https://doi.org/10.1016/j.jmrt.2023.11.252
Received 18 July 2023; Received in revised form 8 October 2023; Accepted 27 November 2023
Available online 30 November 2023

fluid, the tendency to show localized corrosion is also common for 316L SS biomedical implants [13]. Furthermore, it exhibits the drawback of becoming brittle when subjected to prolonged high-temperature exposure in a carbonaceous environment, as carbon is responsible for Cr depletion and sensitization [14]. Such Cr depletion from the matrix makes the implant part highly vulnerable to corrosion [15]. The addition of Ti can negate the negative effects of residual carbon with increased biocompatibility [16].

Ti reacts with carbons and nitrogen to form titanium carbide (TiC), nitride (TiN), and carbonitride (TiCN) [17]. These carbides and nitrides are more stable than chromium carbides and prevent Cr depletion. TiC is famous for its excellent resistance from intergranular corrosion, stress corrosion cracking, and creep [16]. A thin, stable oxide layer usually forms on the Ti's surface, providing a protective barrier against the surrounding, even in harsh environments [18]. Moreover, Ti ions, if released in the body, do not show a cytotoxic response and keep a safe balance of positive (+ve) and negative (-ve) charges by dissolving the hydroxyl group (-OH) from the surface passivation layer [19]. The stability of the passivation layer is affected by its surroundings, and its composition can be altered over time. The layer is not entirely stable as it is not completely oxidized and acts as a reactive site of forming calcium phosphate ($Ca_3(PO_4)_2$) [20], hence increasing biocompatibility and active osseointegration. Researchers produced as cast [21,22] and selective laser melted (SLM) [23] Ti-stabilized 316L SS alloys where Ti and 316L were melted completely and homogenized. However, in PIM, the uniformly dispersed Ti-316L SS powders have been sintered below their melting temperature, where Ti is not melted completely but diffused and bonded with the matrix by its outer layer. Therefore, Ti particles act as a reinforcement, initiate nucleation in the 316L SS matrix, and strengthen the alloy.

In the human body, bones are not in direct contact with other bones, and not all joints have a wide range of movements. Synovial joints can have long movements; however, these movements have been smoothened and stabilized by articular cartilage, synovial fluid, ligaments, joint capsule, etc. Articular cartilage has the highest surface roughness in direct contact during body movements. Siddharth et al. investigated the articular cartilage roughness and measured the value from a range of 82.6 nm to 1.6 μm. Also, the hardness for high and low-weight-bearing cartilage is 4.46 ± 4.44 and 0.317 ± 0.397, respectively [24]. Consequently, frictional wear of implants due to direct bone contact is negligible. However, implants that need to have metallic ball-socket joints, such as total hip joint, shoulder joint, knee joint, and ball (i.e., femoral head), have experienced the opposite directional sliding motion against the socket (acetabular component). Thus, sliding wear resistance property is essential for them. Also, these implants are mainly under compressive and flexural load inside the body. The required strength of implants can be identified by comparing them with the load-carrying bones in the human body. The tibia is the most strengthful bone, having ultimate tensile strength and ultimate bending of 159 MPa and 281 MPa, respectively [25]. Also, cortical bone has a tensile strength of 90 MPa [26], compressive yield strength (CYS) of 130–180 MPa, and Young's modulus (YM) of 4–30 GPa [27]. On that note, an orthopedic implant must have yield strength (YS) of at least 300 MPa [28]. 316L SS is well-suited for fulfilling this requirement and can be used for such applications. However, the YM of 316L SS (200 GPa) is much higher than bone YM (10–40 GPa) [8,29,30]; the stress-shielding effect, osteopenia, and re-fractures are most likely to occur because of the mismatch of YM between bone and metal implant [31–33]. Therefore, alloying elements should keep the implant modulus closer to the bone modulus to overcome these problems.

This study examines how the inclusion of 1, 3, and 5 vol% (0.87, 2.50, and 4.20 wt%, respectively) of Ti affects the physical and mechanical properties of 316L SS sintered under vacuum conditions. A higher sintering temperature aids in the diffusion of materials within the matrix and promotes increased densification [34]. For that reason, three different sintering temperatures, 1300 °C, 1350 °C, and 1380 °C, have also been considered to develop a densified part with improved mechanical properties. In the end, an improvised wear resistance test was performed to evaluate the wear coefficient running on an opposite directional sliding motion mimicking the body movement. This new alloy may signify a growing inclination toward exploring economic, non-toxic, biocompatible, and mechanically viable materials for biomedical applications.

2. Materials and methods

Three different mixing compositions were prepared with 1, 3, and 5 vol% Ti (purity 98 %) and 316L SS (purity 99.5 %). In this experiment, spherical shape gas-atomized 316L SS (Alfa Aesar, UK) and irregularly shaped Ti powder (Alfa Aesar, UK) with particle sizes $D_{50} < 5$ μm, $D_{90} <$ 10 μm and $D_{50} < 18$ μm, $D_{90} < 32$ μm is used, respectively. A Hitachi TM3000 scanning electron microscope (SEM) is used to determine the morphology of powders, as shown in Fig. 1, and energy dispersive spectroscopy (EDS) is used to identify the chemical compositions in Table 1.

The fabrication starts with dry mixing Ti powder with 316L SS using a shaker mixture (WAB T2F Turbula) for 30 min, followed by a Z-blade sigma mixture at a mixing temperature of 150 °C and 50 rpm rotational speed with binders for 60 min to prepare feedstocks. Binders consist of paraffin wax (PW), polypropylene (PP), and stearic acid (SA) with 70 vol %, 25 vol%, and 5 vol%, respectively. PW has been used to achieve improved flowability, PP works as a backbone binder and provides green part strength, and SA improves wettability and sufficient coating on powders. A 65-vol.% powder loading is used for each feedstock, and a vertical injection molding machine (MCP 100 KSA) has been employed with a 4-bar injection pressure with 10 s injection time at 175 °C to fabricate green parts. Spherical 316L SS and irregular shape Ti powder ensure sufficient green part strength. Afterward, the green parts were carried through solvent debinding using n-heptane in a Memmert water bath for 420 min at 60 °C. A prolonged debinding process helped remove some primary binders and effectively created a porous channel to remove secondary binders during the thermal debinding process. In the next step, samples were dried at 60 °C in a forced convection oven (MTI DHG-9070V) for 24 h, followed by thermal debinding. The thermal debinding and sintering were carried out in a single cycle, shown in Fig. 2, in a tube furnace (GSL 1700X) under a vacuum atmosphere. The vacuum atmosphere prevents the sample from being oxidized, and such negative pressure sucks the evaporated fumes out of the specimen, thus helping densification.

In the process, injected parts, solvent-debonded parts, and sintered parts are named as "green part", "brown part", and "silver part", respectively. After completing the sintering cycles, sintered parts with no visible defects were produced. To avoid the long name from now on samples will be addressed, 1 % Ti-316L @1300 °C (S1), 1 % Ti-316L @1350 °C (S2), 1 % Ti-316L @1380 °C (S3), 3 % Ti −316L @1300 °C (S4), 3 % Ti-316L @1350 °C (S5), 3 % Ti-316L @1380 °C (S6), 5 % Ti-316L @1300 °C (S7), 5 % Ti-316L @1350 °C (S8), 5 % Ti-316L @1380 °C (S9).

3. Results and discussion

3.1. Defects and density

The density was measured following Archimedes' principle (ASTM B962-17) on a density meter (Mettler Toledo AX205). The mass, mass loss, and relative density of samples are listed with their shrinkage in Table 2.

The density of the sintered part depends on the sintering temperature. Sintered at 1380 °C produced higher density, mass loss, and shrinkage for the identical Ti content. 3 vol% Ti @ 1380 °C has shown the highest 96.11 % relative density (RD) and 88.70 % green density. Hwang et al. [35] debonded the sample in a hydrogen atmosphere and

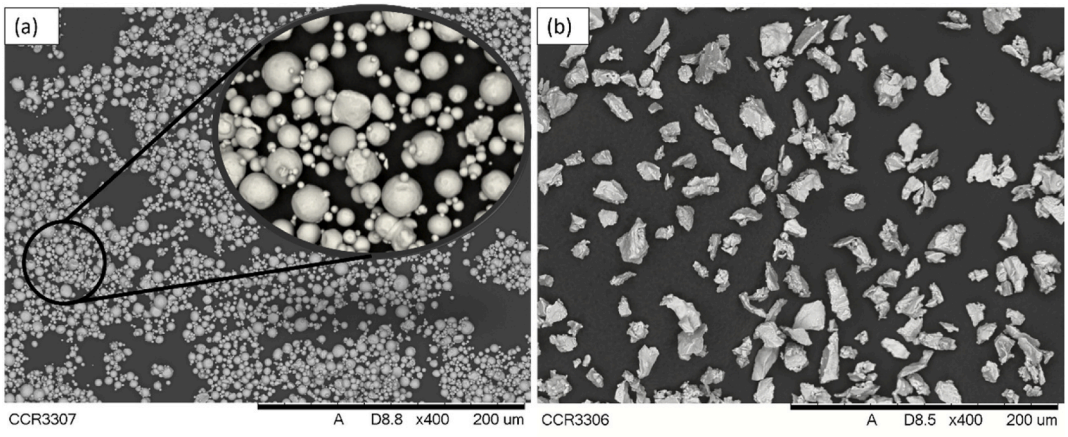

Fig. 1. SEM images of (a) 316L SS, and (b) Ti powder.

Table 1
Compositions (wt.%) of gas-atomized 316L SS and Ti powder.

Powders/elements	Ti	Cr	Ni	Mn	Si	Mo	C	P	S	Fe
316L	–	16.97	12.343	1.368	1.258	2.20	0.03	≤0.045	≤0.03	Bal.
Ti	98.48	–	–	1.50	–	–	0.02	–	–	–

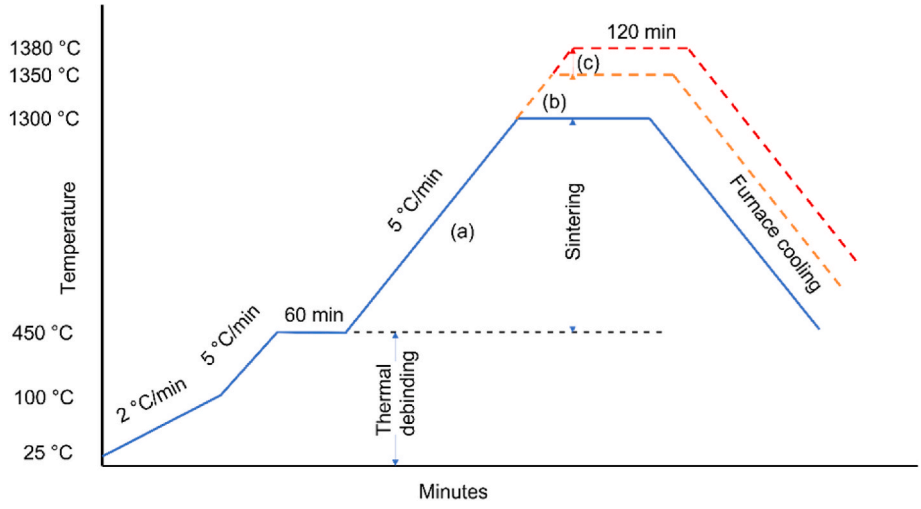

Fig. 2. Thermal debinding and sintering cycle. Thermal debinding takes place at 450 °C. Three sintering temperatures of (a) 1300 °C, (b) 1350 °C, and (c) 1380 °C have been adopted with 2 h dwell time.

Table 2
Mass loss, relative density, and shrinkage of parts.

Sample	Mass			Total mass loss %	Relative Density		Shrinkage %
	Green part (g)	Brown part (g)	Silver part (g)		Green %	Sintered %	
S1	14.29	13.59	13.47	5.79	88.51	92.29	12.91
S2	14.22	13.52	13.39	5.83	88.48	93.41	13.86
S3	14.23	13.53	13.38	5.97	88.51	94.12	13.91
S4	14.28	13.62	13.43	5.95	88.69	94.86	13.70
S5	14.14	13.41	13.29	5.90	88.73	95.18	13.37
S6	14.27	13.62	13.41	0.60	88.70	96.11	13.79
S7	13.96	13.26	13.13	5.95	88.64	93.63	13.36
S8	13.88	13.18	13.05	5.98	88.63	95.29	13.45
S9	14.01	13.30	13.18	5.99	88.64	95.73	13.49

sintered it in a vacuum, achieving 94.62 % RD for 316L SS. Another research has been conducted by Shieddieque et al. [36], where they achieved only 87 % RD of 17–4 PH SS sintered at 1360 °C with a 1.5 h holding time. Therefore, it indicates that adding Ti helps to densify the sintered sample by increasing the packing factors and promoting the sintering mechanism by solid-state diffusion. Ti percentage from 3 vol%

to 5 vol% reduces green density for all samples. Initially, it can be attributed to the irregular Ti powders, which elevate viscosity and reduce mold flowability, thus creating voids between particles. Up to a Ti content of 3 vol%, the small spherical 316L powders, with their wide powder distribution, effectively fill the gaps between the Ti and 316L powder. However, an excess of Ti surpasses the threshold limit, hindering the attainment of a tightly packed green part. Moreover, the density of both the green and sintered parts exhibits a correlation, as the sintered density depends on the residual voids present in the green part. Also, captive fume generated by low molecular weight SA due to thermal degradation and evaporation contributes to the creation of less dense green parts [37].

3.2. XRD

XRD analysis has been performed on an X-ray diffractometer (Panalytical X-Pert^3 Powder) using Cu-Kα radiation. The scan rate was 0.02 deg/step, and the scan range was 10°–110° to ensure complete coverage. The Xpert High Score Plus software was used to identify and verify the compounds with published works [38–40]. In this experiment, XRD patterns were analyzed only for 1, 3, and 5 vol% Ti samples sintered at 1350 °C as the intermetallics remained the same below 1400 °C [41,42]. Fig. 3 shows the patterns with the list of intermetallics. Both ferrite and austenite phases have been detected. Increased Ti content stabilizes the austenite phase at room temperature as no ferrite peak was observed at 79.6° in 3 and 5 vol% Ti samples. The XRD patterns for samples containing 3 and 5 vol% of titanium (Ti) detected the presence of α-Ti (JCPD 00-044-1294), while 5 vol% Ti indicated the presence of β-Ti (JCPD 01-071-9955). Notably, the 5 vol% Ti samples exhibited higher intensity at $2\theta = 44°$ compared to those with 1 and 3 vol% Ti, signifying the presence of α-Ti with a distinct (101) diffraction peak. Additionally, a slightly shifted peak at $2\theta = 50.3°$ and 59.2° confirmed the existence of (200) and (211) beta-stabilized Ti in the S5 and S8 samples, respectively. It's worth mentioning that no TiC peaks were identified in any of the XRD patterns, except for a minor peak corresponding to silicon carbide (SiC). Titanium silicon carbide (Ti_3SiC_2), and cubic $Cr_{23}C_6$ were identified in 1 and 3 vol% Ti samples, and orthorhombic Cr_7C_3 (JCPDS card 36–1482) has been observed in every XRD analysis. A wider peak and a peak with twin shoulders were observed in S2 and S8, respectively, at 96.6°, indicating the presence of (305) Cr_3C_2. Due to the fact of silicon in the 316L matrix, Ti_3SiC_2 is likely to form rather than TiC. Thus, a more prominent peak of Ti_3SiC_2 was detected in the 1 and 3 vol% Ti. Additionally, as the percentage of Ti increases, there is a reduction in Cr depletion in the form of carbides. These intermetallic compounds play a role in strengthening the austenitic matrix while also introducing some brittleness. Since Ti is a strong carbide former, a small portion of C atoms diffused inside Ti may lower the scope of Cr and Si carbide formation [43]. Another perspective to consider is that TiC may have formed within the matrix, but its presence in small quantities renders the TiC spikes practically imperceptible, given the overwhelming presence of high-intensity major constituent elements.

3.3. Optical microstructures

The samples were ground through 180–2400 grit emery paper, further polished by 3-μm polycrystalline diamond suspension, and electric etched at 3.5 V for 2 min in a 10 % oxalic acid solution. An optical microscope (Leica DM2700 P) was used to observe the microstructure shown in Fig. 4. Grain boundaries sintered at 1300 °C for S1 were not visible due to insufficient grain growth and remaining pores, and the rest of the samples have formed an equiaxed grain. During the crystallization process, a lower sintering temperature failed to facilitate sufficient diffusion within the matrix and could not mitigate the pores fully (as depicted in Fig. 3d), which resulted from the debinding stages. The inclusion of Ti enhances solid solubility, which, in turn, can exert an influence on grain boundary mobility, thereby influencing alterations in

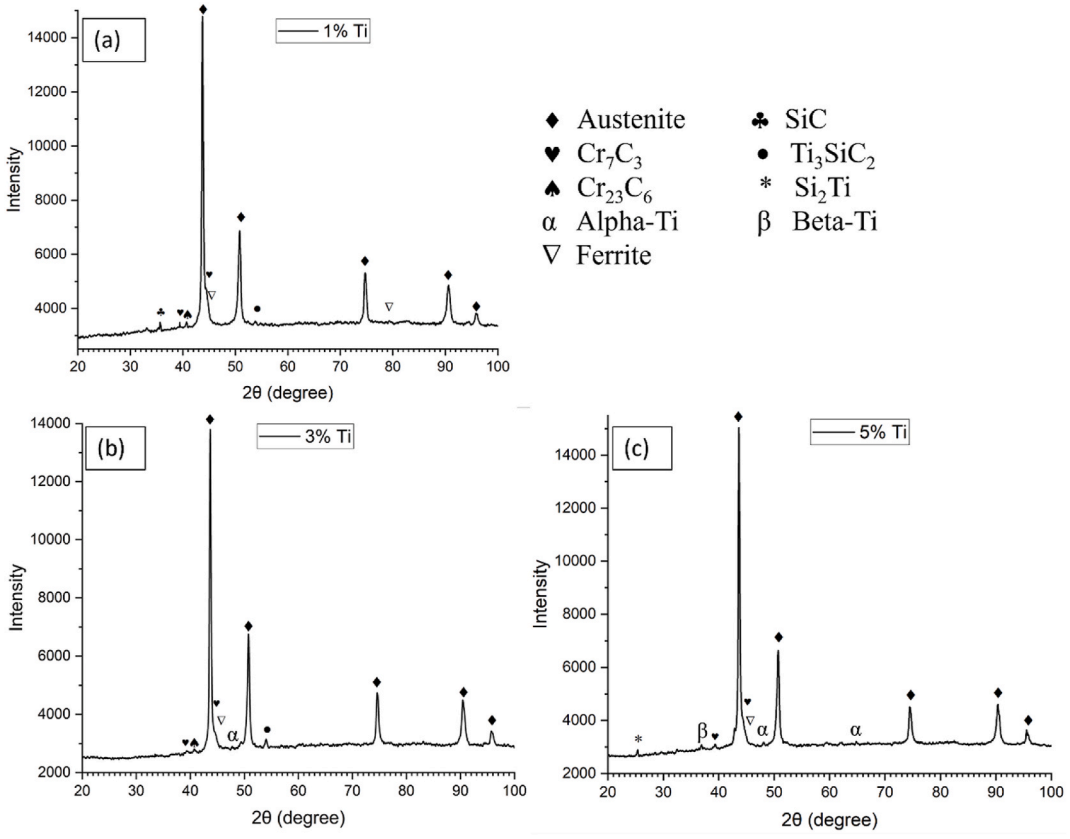

Fig. 3. XRD patterns of (a) S2 (b) S5, and (c) S8 samples.

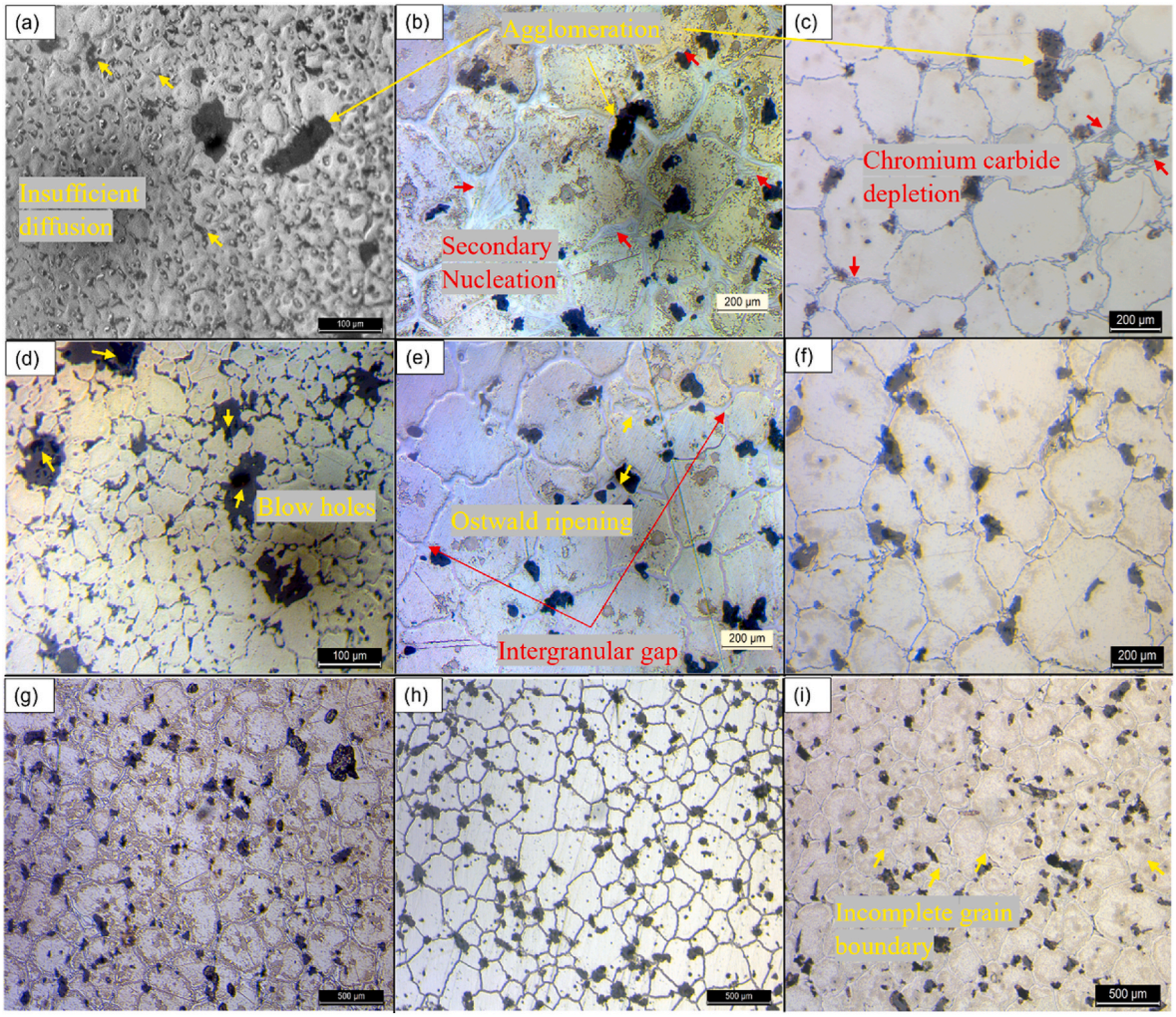

Fig. 4. Optical microscopic (OM) image of (a) S1, (b) S2, (c) S3, (d) S4, (e) S5, (f) S6, (g) S7, (h) S8, and (i) S9.

grain growth during the sintering process. Also, Ti introduces energy differences that can impact both grain boundary motion and grain boundary characteristics. Therefore, a noticeable grain boundary appeared in samples S4 and S7, even though they were sintered at the same temperature as S1.

Samples sintered at 1350 °C presented an intergranular gap between grain boundaries and an interfacial gap between the Ti and matrix. In the S2 sample, secondary gain nucleation and incomplete crystallization were observed. Additionally, near the Ti particles in S5, there was ongoing Ostwald ripening (OR) driven by significant concentration gradients [44]. These factors fundamentally contributed to the presence of intergranular gaps. Since OR is a time-dependent process and owing to the increased solid solubility capacity of Ti, the ripening process becomes faster. Thus, relatively smaller intergranular gaps were observed in the S8 sample. Conversely, Complete grain growth has been observed in the samples sintered at 1380 °C, with no interfacial gap detected between the Ti and the matrix.

The average grain size and standard deviation have been calculated and given in Fig. 5. Due to the insufficient diffusion and no conspicuous boundaries, the grain size of S1 cannot be measured. Higher sintering temperature ensures more grain boundary diffusion and grain growth. On the contrary, Ti particles work as a nucleation site and decrease the grain size. Therefore, the average grain size increases with the increase of sintering temperature and decreases with the increment of Ti content. The standard deviation (std. dev.) of grain size also shows a similar pattern except for S7. On the other hand, the variation in grain size can

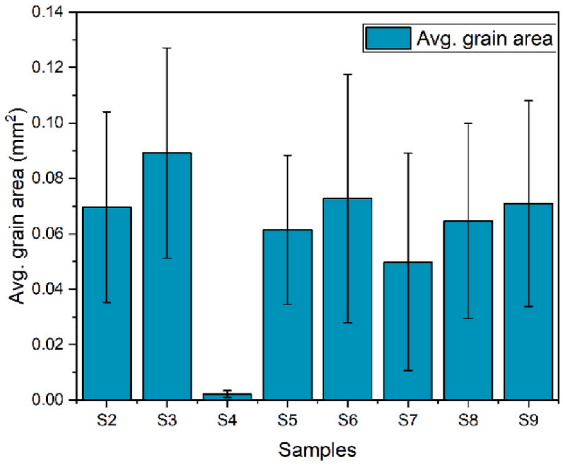

Fig. 5. Average grain size (area) and corresponding standard deviation of samples S2–S9.

be attributed to agglomeration and uneven distribution. As illustrated in Fig. 4, the clustering of Ti particles was due to their irregular shape and higher percentage, resulting in more pronounced clustering. This phenomenon arises from the presence of surface irregularities, such as protrusions, concavities, or rough textures, which foster robust

interparticle interactions and adhesive forces, leading to particle cohesion upon contact, mainly because of its enlarged surface area.

3.4. SEM and EDS

Due to the intergranular and transgranular Cr-enriched carbide precipitation and insufficient diffusion, fuzzy grain structure can be seen in S1 and S4 samples. In Fig. 6, the SEM and EDS results of the samples are presented to gain insight into the compounds formed within the matrix. The presence of chromium carbide precipitation was confirmed for all samples through EDS mapping. Notably, chromium carbide precipitate was observed along grain boundaries at higher sintering temperatures, whereas the lowest precipitation was observed in S6. Unlike the remaining samples, a severe chromium depletion was noted in the S3 sample, leading to the formation of a network-like secondary chromium phase along the grain boundaries (refer to Fig. 6c). This was attributed to the extremely high sintering temperature (1380 °C). Despite identical sintering temperatures, narrower chromium networks were observed for S6 and S9. This phenomenon underscores the role of Ti in mitigating chromium depletion at elevated temperatures.

The crystal structure of chromium carbides depends on the stoichiometric ratio of carbon to Cr. Cubic $Cr_{23}C_6$ is likely formed with a high percentage of Cr, while increased amounts of carbon help to form hexagonal Cr_3C_2 and Cr_7C_3 of orthorhombic and hexagonal Ru_7B_3-like structures [39,45,46]. Although irregular primary Cr_7C_3 with protrusion tendency and head-tail linkage was observed in Fig. 6 (a) [40], XRD did not provide any supportive pattern. However, carbides work as a heterogeneous nucleation zone, restricting grain growth [47]. Few pores are visible on the matrix due to the trapped gas produced from the evaporation of surfactant during the injection. These pores could not be fully closed during the sintering since the pore size of the brown part exceeds the size of the particles used. Under such circumstances, the pores move inwardly into the grain. The filling of the pores through grain growth is obstructed due to the low bulk (lattice) diffusion compared to grain boundary diffusion [48], which results in the formation of voids, thus ultimately lowering the density. Some pores are also observed on the Ti particles, especially samples sintered at 1380 °C. Agglomeration of Ti particles arises from high surface energy. Moreover, higher sintering temperatures exacerbate this effect, resulting in the formation of agglomerates and leaving behind pores (see Fig. 6 (i))

Silicon (Si) segregation from the matrix occurred during the sintering, especially for higher temperatures and Ti-contained samples. Since

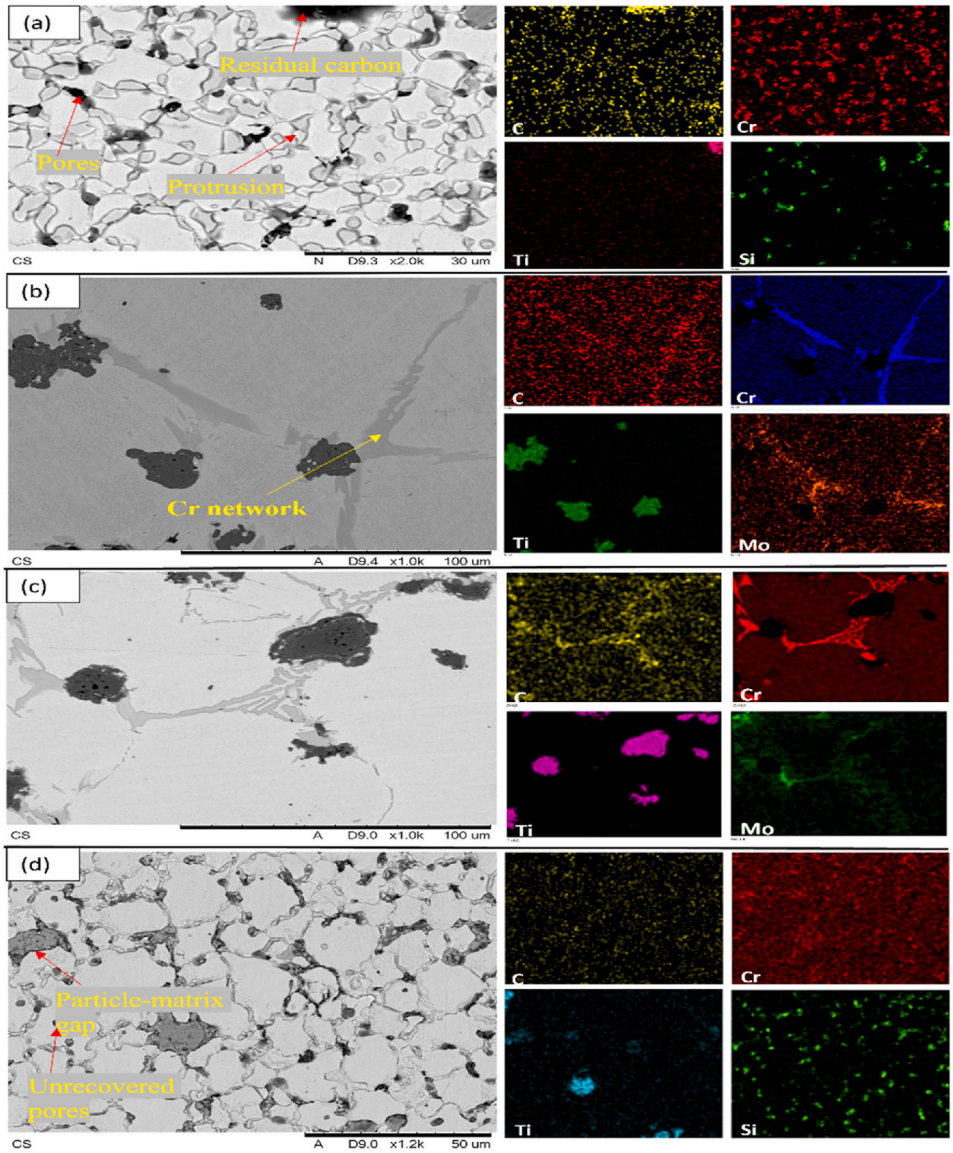

Fig. 6. SEM micrograph with EDS mapping of (a) S1, (b) S2, (c) S3, (d) S4, (e) S5, (f) S6, (g) S7, (h) S8, and (i) S9 samples.

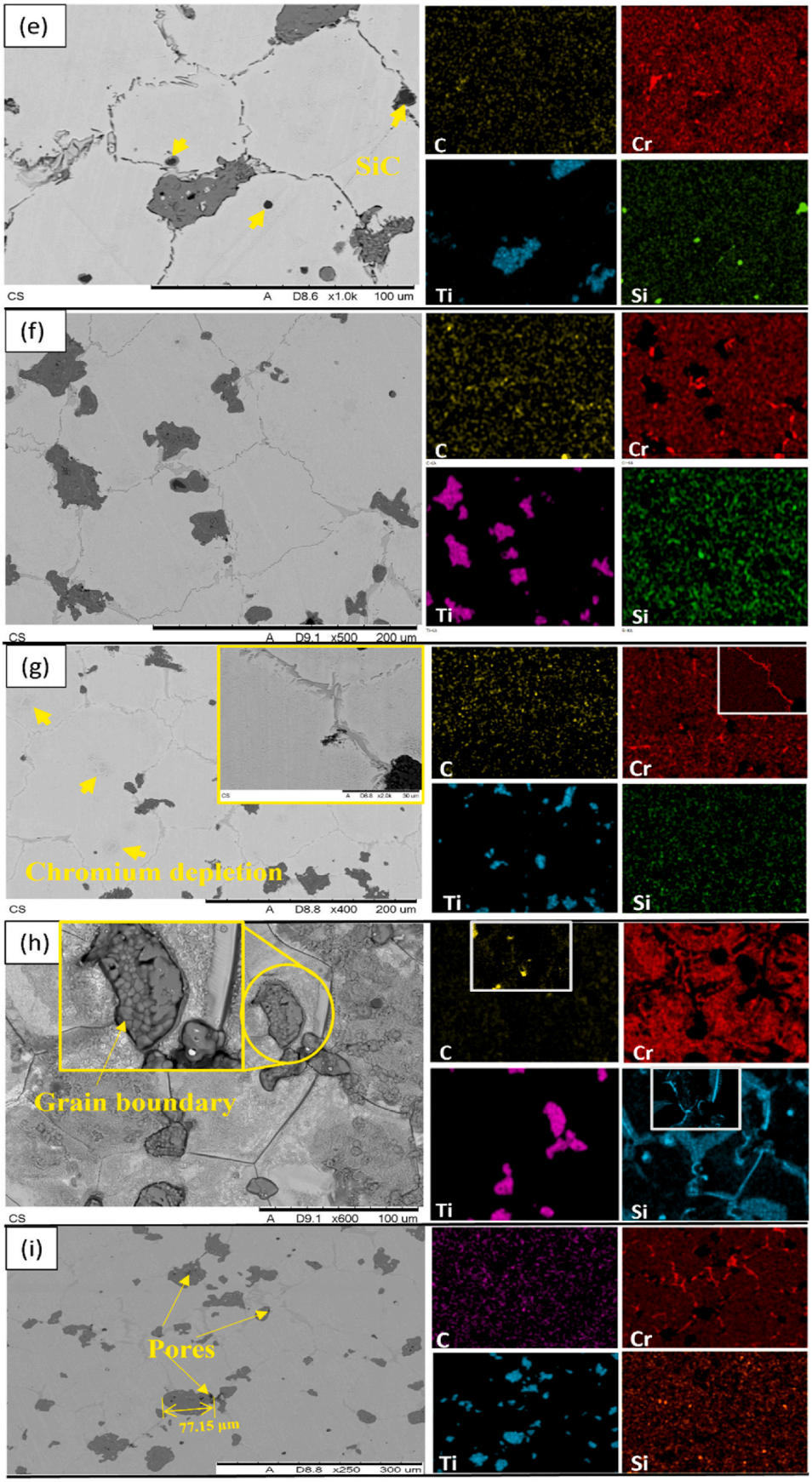

Fig. 6. (*continued*).

Si has a lower solubility in solids, it tends to migrate to higher energy regions like grain boundaries [49]. An apparent Si banding has been observed (EDS image of Fig. 6 (h)) on the grain boundaries and the vicinity of Ti particles. This accumulation forms silicides and makes the sample brittle. The attending silicon also reacts with Ti and carbon to form titanium disilicide ($TiSi_2$) (JCPDS: 01-085-0879) and silicon carbide (SiC). SiC is an exceptionally hard material [50], and the trace was found in XRD. Additionally, SiC can be identified by visually inspecting the microstructure as it often forms on the grain boundary and shows weaker bonding with visible gaps to the particle-matrix interface (Fig. 6 (e)) [51]. For $TiSi_2$, the activation energy is lower than Ti_5Si_3, and $TiSi_2$ preferably develops in solid-state and solid-liquid diffusion, respectively. Consequently, below the eutectic point (1330 °C) of Ti–Si, the tendency of $TiSi_2$ growth is trivial [52]. However, at a higher Ti percentage (5 vol%) and higher sintering temperature (1350 °C), the $TiSi_2$ spike has been well identified in XRD.

The residual carbon works as a liquid-forming additive and diffuses the lattice structure to construct the Nowotny phases $Ti_5Si_3C_x$ [28,29] and the Max phase Ti_3SiC_2 [53]. These intermetallics have been developed by the thermochemical reaction of Ti and SiC at a higher temperature ranging from 1260 °C to 1400 °C [42]. A prominent spike of the Max phase has been observed in the 3 vol% Ti sample. Visual evidence suggests a nodule-like retained β-Ti micro-gains form on Ti particles (Fig. 6 (h)) [49]. This notion can be justified by observing the constituent elements (Fe, Cr, Ni, Mn, and Si) of 316L SS. These elements are known as beta-stabilizers with minimal solid solubility in Ti [54]. According to Bania, alloys with more than 10 wt% molybdenum equivalency (Mo eq.) could retain the β-Ti phase since Mo eq. of 316L SS constituents are: Mo = 1.0, Fe = 1.23, Cr = 1.1, Ni = 1.67, Mn = 1.42, Si = 0.99 [55]. Also, the XRD analysis detected the β phase. Irrefutably, the inclusion of Ti reverses the effect of residual carbon to some extent, although carbides and silicides cost the ductility and make samples brittle.

3.5. Macro, micro, and nano hardness

Three different hardness tests, Rockwell, micro-Vickers, and nano-indentation have been performed to understand the macro, micro, and nano performance. The Rockwell hardness test (HRA scale) has been performed using a cone-shaped diamond indenter and 60kgf load on the Mitutoyo universal hardness tester. For Vickers hardness (Model: LM247AT), a pyramidal shape tip with 500gf and 10 s dwell time has executed, and for nano-indentation (NI), Anton Paar NHT^3 nanoindenter has used with a maximum force of 80 mN, loading-unloading rate of 160 mN/min, and dwell time of 10 s. The Oliver–Pharr method has been employed to measure the hardness and modulus. Microhardness and NI data (H_{IT}) were collected from two distinct locations. The first location was consistent for both tests and was situated on the matrix where no Ti particles were present. However, for the second location, microhardness measurements were taken on the Ti particles themselves, while NI measurements were obtained from the interface of both Ti and the matrix. The average value of at least four readings for macro and micro hardness (Fig. 7) and ten readings for nano-indentation has been obtained (Table 3) and enlisted. NI provides the indentation modulus (E_{IT}), indentation creep (C_{IT}), and equivalent Vickers hardness (HV_{IT}) along with the hardness value.

In the Rockwell and Vickers test, monolithic 316L stainless steel usually shows a hardness of around 50 HRA and 155 HV, respectively [56]. However, higher hardness values were observed in this study. The hardness increased with the increase of Ti particles and sintering temperature. The highest and the lowest HRA values recorded were 61.3 and 54.7 for the S9 and S1, respectively, although the values were not increased significantly for similar sintering temperatures with varied Ti content. Similarly, the micro-Vickers test displayed a similar trend, with a notable increase observed when sintering 5 vol% Ti at 1350 °C as compared to 1300 °C, resulting in an increase in hardness from 255.4 HV to 280.3 HV. A minor difference in hardness was observed between specimens sintered at 1350 °C and 1380 °C, suggesting that most of the diffusion processes and intermetallics formation were completed at 1350 °C. The hardness values near the Ti particles consistently exceeded those of the matrix. However, the values remained relatively uniform from S1 to S7 samples, exhibiting minimal variation concerning Ti particles and sintering temperature. Only in the cases of S8 and S9 was a substantial increase in average hardness observed, measuring 313.4 HV and 323.2 HV, respectively. Increased Ti present in the matrix at higher temperatures forms $TiSi_2$ that might give a boost to the hardness. Moreover, the hardness value varied more in 1 and 3 vol% Ti samples compared to 5 vol% Ti. This behavior indicates that the hardness value is not uniform throughout the matrices. The formation of chromium carbide, titanium carbide, and silicides increases the local hardness. The variable presence of such particles gives hardness variation. Higher sintering temperature allows more homogeneous distribution and migration of second solid phases towards the grain boundary as well as the interface of Ti-matrix, thus increasing hardness value near the Ti particles. To verify such behavior, micro indentation morphology and a nano-indentation test on the vicinity of the Ti-matrix interface have been performed.

Fig. 8 provides the SEM image of micro-hardness indentation profile, where depleted chromium carbide consistently displays lateral cracks (point 2) in all samples except for S1. However, the renowned borderline

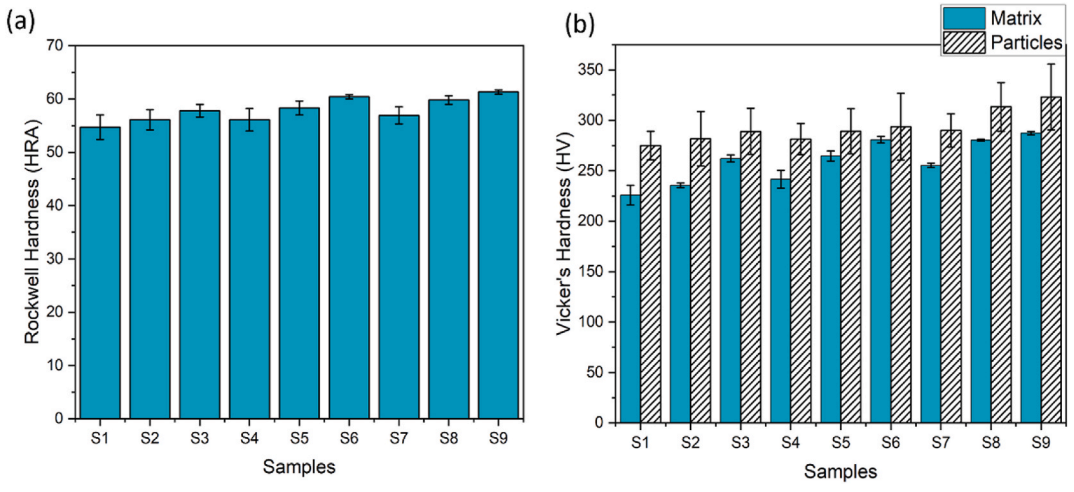

Fig. 7. Hardness value with a standard deviation of (a) Rockwell (HRA) and (b) Micro-Vickers (HV).

Table 3
Nano-indentation data of matrix and Ti particles-matrix interface.

Sample	Matrix					Ti-Matrix Interface				
	H_{IT} (GPa)	HV_{IT}	E_{IT} (GPa)	C_{IT} (%)	H_{IT}^3/E_{IT}^2	H_{IT} (GPa)	HV_{IT}	E_{IT} (GPa)	C_{IT} (%)	H_{IT}^3/E_{IT}^2
S1	5.46	505.5	233.8	1.68	0.003	10.98	1017	213.1	−1.78	0.029
S2	4.57	424.0	164.5	1.84	0.004	13.98	1295	159.9	−2.53	0.106
S3	4.31	399.3	157.6	2.41	0.003	15.34	1421	116.7	−3.00	0.265
S4	5.67	525.4	189.3	2.37	0.005	11.35	1051	188.1	−1.92	0.041
S5	4.43	410.6	149.3	2.78	0.004	15.05	1394	117.2	−3.12	0.248
S6	4.01	371.4	145.9	2.47	0.003	18.02	1669	89.3	−3.68	0.733
S7	5.11	473.5	156.4	2.32	0.005	12.56	1163	154.5	−2.74	0.083
S8	4.23	391.9	142.9	1.99	0.004	14.58	1350	107.6	−3.99	0.267
S9	3.85	356.8	129.1	1.55	0.003	20.82	1928	100.4	−5.40	0.895

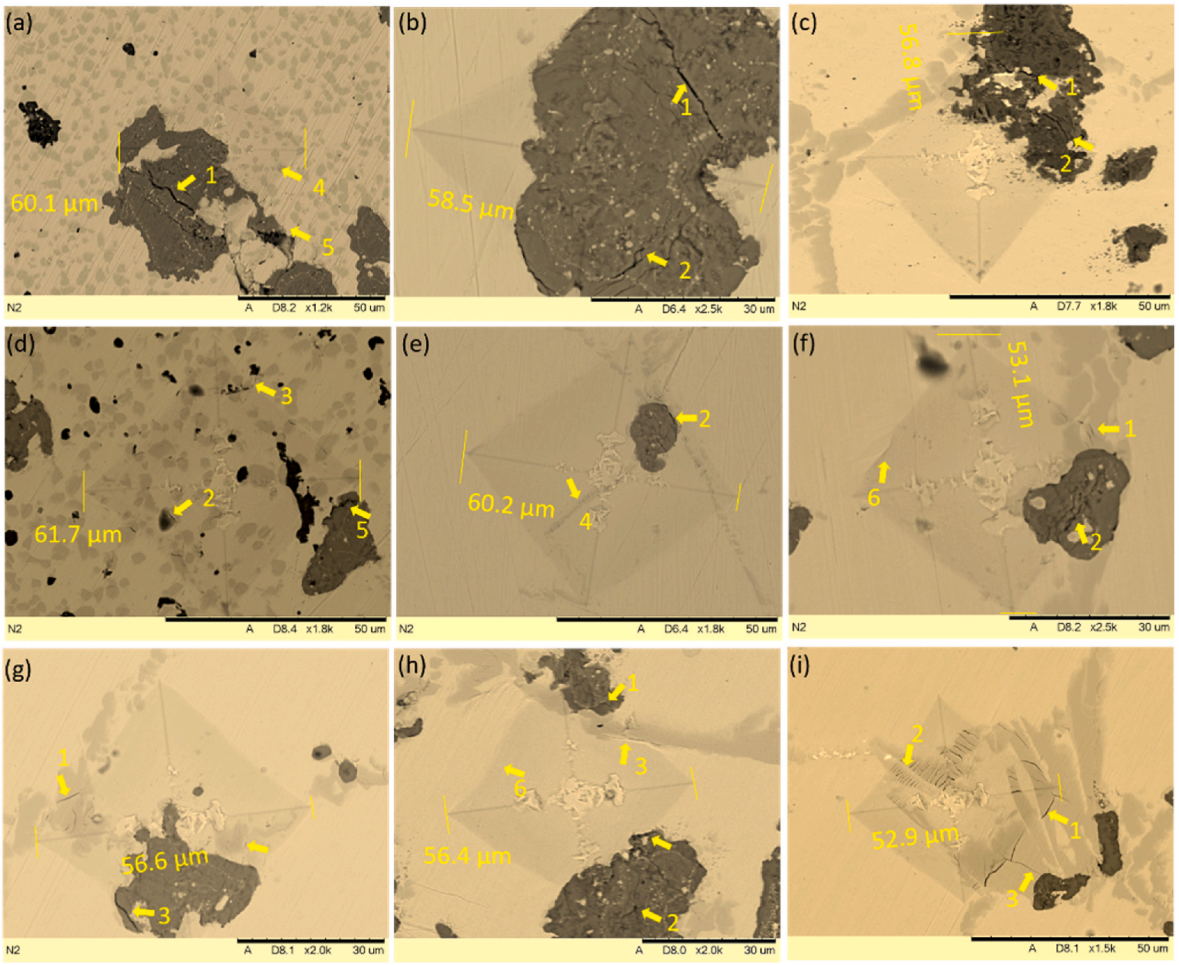

Fig. 8. SEM image of micro-hardness indentation of (a) S1, (b) S2, (c) S3, (d) S4, (e) S5, (f) S6, (g) S7, (h) S8, and (i) S9. Point 1 indicates the borderline crack, 2 for lateral crack, 3 for radial crack, 4 for micro-cracks, 5 for stress-induced crack outside indentation, and 6 for the spring-back effect.

crack (point 1) on Ti indicates a brittle fracture. Moreover, in every indentation where Ti was compressed under the indenter, a multi-stack lateral crack was observed. Interestingly, as the sintering temperature increased, the extent of fracture in the Ti specimens also increased. Stress-induced cracking was observed in S1 and S4 samples because of the structural weakness due to insufficient diffusion. The diagonal length of indentation was getting shorter with the increase of depleted chromium at higher sintering temperatures. This trend suggests a brittle radial crack (point 3) in the chromium carbide second phase, particularly in the S9 samples, indicating high brittleness within these samples. Also, a series of parallel lateral cracks along the shear plane were observed in Fig. 8 (i). Samples S6 and S8 exhibited edge distortion and a spring-back effect without the generation of cracks. This phenomenon highlights the local elastic nature of these samples, where residual stresses accumulate during indentation without causing fracture. This distortion predominantly occurred near the centre of the grain, at some distance from the Ti particles. This observation may provide insights into the material's stiffness. However, these properties are not consistent throughout, suggesting a composition gradient within the matrix.

A nano-indentation test has been carried out to understand the previous hardness behavior by taking hardness data from a precise and niche location. It can also analyze the elastic behavior at different locations with nano-hardness and creep properties. All the experimental data of the matrix and matrix-particles interface have been recorded in Table 3. When it comes to the matrix, S4 sample has shown the highest NI hardness of 6.34 GPa, and S9 obtained the lowest value of 3.85 GPa.

In each level of Ti content, a consistent decrease in nano-hardness was observed as the sintering temperature increased. This trend is indicative of the intricate relationship between nano-hardness, crystal plane orientation, and orientation-dependent diffusion coefficients [57], especially in anisotropic materials like titanium. Hence, the sintering temperature and inclusion of Ti have great influences on nano-hardness. In this study, the gradual Ti diffusion reduced the hardness value and elastic modulus, which is the opposite of the findings of macro or microhardness. Ti has a lower hardness than 316L SS, and the proper diffusion of Ti reduces the hardness at the nanoscale level. The NI test also provided the creep (C_{IT}) properties, although no clear relation was observed for the matrices. The elastic property can be analyzed by calculating the resistance to plastic deformation, H_{IT}^3/E_{IT}^2. A higher value represents more resistance to plastic deformation [58]. Therefore, a lower E_{IT} is essential as it indicates the distribution of applied force to a vast area, although it conflicts with the orthodox theory of linear-elastic fracture mechanics. The resistance to plastic deformation (RPD) was negligible for matrices, and all the samples showed creep behavior under the constant load.

Contrarily, the drastic hardness improves with the fall-off elastic value for the reading taken on the particles-matrix interface. Each sample scored over 1000 $HV_{IT,}$ indicating the presence of extremely hard brittle particles. In EDS mapping, it was observed and mentioned earlier that Si and C were segregated from the matrix and accumulated at the edge of Ti particles. These Si and carbon formed SiC, TiC, and complex Ti_3SiC_2 ceramic intermetallics at high temperatures, thus increasing the HV_{IT} value. This diffused layer thickness increased with the sintering temperature, and all the highest HV_{IT} were noticed at 1380 °C. But, the undiffused layers on the vicinity of intermetallics might give a cushioning effect and help reduce the elastic modulus. A very high RPD value and negative creep value give the indication of a hard phase present. Sintering at higher temperatures with high Ti contents increases substantial elastic properties with a high H_{IT}^3/E_{IT}^2 ratio as the silicon and carbon accumulation and formation of intermetallics increase.

Fig. 9 portrays a model force vs penetration graph of the NI test conducted on the S5 sample, showing the results for both the matrix and particle regions. The unloading curve for the Ti-matrix interface indicates elastic deformation, whereas the matrix shows plastic deformation, and the area under the curve represents the energy dissipation due to plastic deformation. The energy dissipation is inferior for the Ti-matrix interface compared to the matrix.

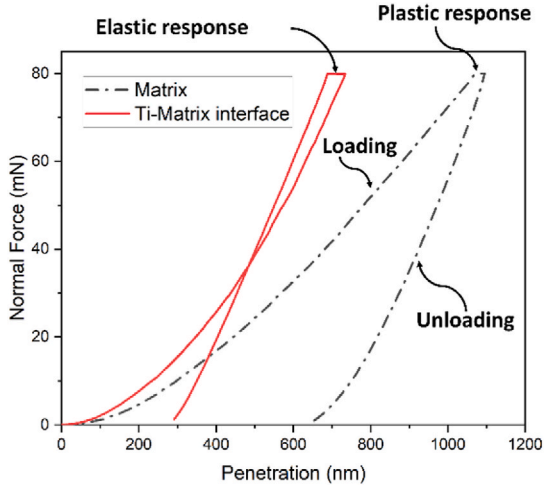

Fig. 9. A model force vs penetration graph of nano-indentation test for both matrix and Ti-matrix interface.

3.6. Tensile test

Tensile tests were performed according to the ASTM E8M standard with a strain rate of 0.008 mm/s at room temperature using a universal testing machine (Amsler Zwick 50 KN). Fig. 10 summarize the tensile test properties. Fig. 10 (a) shows the stress-strain curve, where the x-axis represents the elongation percentage at the breakpoint. All the tested samples showed brittle fractures with less than 5 % elongation. S3 and S5 have exhibited the lowest and highest elongation with a 2.55 ± 0.07 % and 4.82 ± 0.26 % strain, respectively (Fig. 10 c). S5 also showed the highest ultimate tensile strength (UTS) of 444.7 ± 18.8 MPa. 3 vol% Ti samples showed relatively optimal elongation compared to others. Sintering at 1300 °C does not allow sufficient Ti diffusion in the matrix. Furthermore, the lesser densification results reduced strength; thence, S7 showed the lowest UTS of 353.05 ± 20.5 MPa. In contrast, sintering at high 1380 °C results in high-temperature embrittlement due to the segregation and accumulation of carbon, Cr, and silicon in the grain boundaries, which subsequently reacts with carbide-forming elements such as Ti, Cr, and Mo (Fig. 6). C and Si also showed a tendency to accumulate in the vicinity of the Ti particles (Fig. 6 h) and formed brittle phases, which makes weaker interfacial bonding. Thus, during the tension, the brittle phases fracture suddenly and separate the matrix-Ti bonding and concentrate stress. This observation is consistent with the results obtained from the SEM image of micro-indentation (Fig. 8).

Fig. 10 (d) illustrates the YM and YS at 0.2 % offset strain. S4 and S9 have shown the highest and lowest YM of 147.7 GPa and 58.9 GPa, respectively. Increased Ti content with inadequate diffusion at a low sintering temperature (1300 °C) creates weak bonds with the matrix, and Ti stand-alone could work as an interlocking between two grains, thereby preventing the grain boundary sliding during tensile deformation. This effect assists in increasing the YM and restricts the elongation. Sufficient diffusion at 1380 °C temperature ensures matrix-Ti bonding and nullifies the previous effects. Also, Ti agglomeration creates porous Ti lumps inside the matrix and thus can reduce the YM further [59]. Moreover, the formation of β-Ti (already stabilized in the sample and identified by XRD) aids in lowering the modulus [59]. Higher YM is one of the most significant limitations for load-carrying orthopedic biomaterials. Bender et al. [60] observed that a non-porous 316L SS shows as much as 193 GPa YM. On the other hand, Ti–6Al–4V, a commonly used bioimplant material, has shown 110 GPa YM at room temperature [61]. Maity et al. [62] developed a very expensive β-stabilized Ti–35Nb–7Zr–5Ta (wt. %) alloy showing a modulus value of 73 GPa. From this discussion, it can be concluded that the S3, S6 and S9 samples have a suitable modulus for load-carrying biomedical applications.

3.7. Fractography

After the tensile test, the fractured samples were analyzed on SEM to identify the nature of the fracture and in-situ features given in Fig. 11. An evident dimple-like fracture is observed for S1 and S4, and partial dimple-like rupture is noticed for the S7 sample. Although it should indicate the ductile failure, the extensometer reading and the fracture pattern confirm the brittle fracture. This discrepancy can be resolved by considering the sintering temperature. As spherical powder has been used and due to the low-temperature sintering, weak interparticle necking has been torn down by applied tensile stress and leaves a dimple impression, which has been illustrated in Fig. 12. Also, undiffused particles have been observed in S7. As the sintering temperature goes high, a relatively smooth fracture topography (Fig. 11 (c, i)) with the interfacial and micro-crack (Fig. 11 (b, h)) has been observed.

A cleavage fracture observed in S3 indicates a sudden failure, and the interfacial crack between the Ti and the matrix means weak bonding and improper load transfer. Samples sintered at 1380 °C showed minimum Ti-matrix interfacial crack, indicating sufficient diffusion. S5 and S6 showed a compound mixed-mode fracture where a trellis pattern (dimples with ridge) has been noticed. A similar trellis pattern formed in

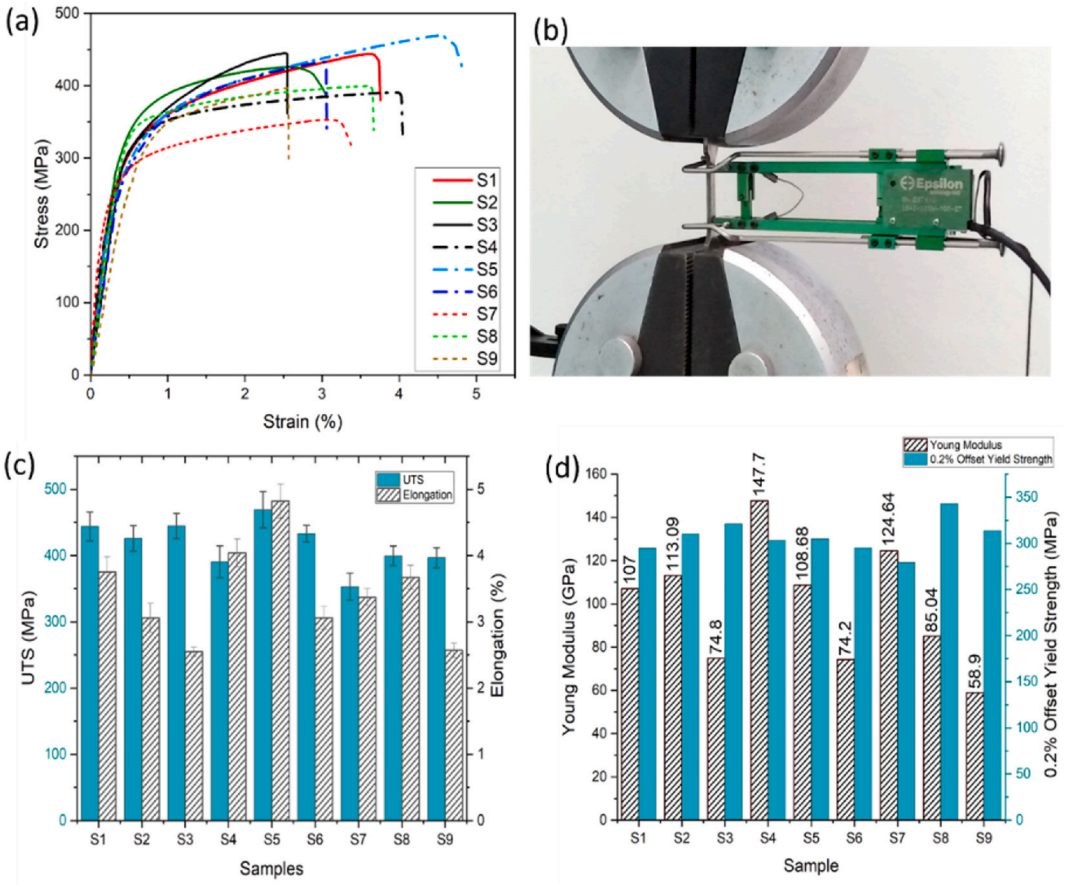

Fig. 10. Tensile properties of samples S1–S9. (a) Stress-strain curves, (b) Test setup, (C) UTS and elongation, and (d) YM with YS at 0.2 % offset strain.

S8 and S9, although the flat ridge gradually became prominent. In S9, a wide, smooth, flat surface demonstrates an extensive slip profile, indicating less plastic deformation and sudden rapture.

3.8. Bending and compression

Bending and compression properties are vital for biomedical implants. In in-vivo conditions, human implants mostly experience flexural or compressive stress. To perform the bending test, samples underwent a three-point bending according to the ASTM E290-14 with a strain rate of 0.008 mm/s at room temperature using a universal testing machine (Amsler Zwick 5 KN). The support distance was 25 mm, and a 10 mm nose diameter was used. As per ISO 3325, Eq. (1) was used to calculate the flexural strength (FS), Where L is the distance between two supports, P is the applied load, w is the width, and t is the thickness.

$$FS = 3L \times P/(2w \times t^2) \quad (1)$$

For the compression test, ASTM E8 was followed with a compressive strain rate of 0.005 inch/min at room temperature. A Cylindrical shape sample of 36 mm in length and 12 mm in diameter was used, and the test was carried out in a universal testing machine (Amsler Zwick 100 KN). Both the bending and compression tests have been performed to examine the flexural and compressive strength on its elastic limit as plastic deformation is unwelcomed for biomedical implants. It is observed from the previous test result that the sample sintered at 1380 °C is densified and showed mostly brittle failure with relatively low YM. Therefore, only samples sintered at 1380 °C were carried out for bending and compression tests to evaluate their flexural yield strength (FYS) and CYS. Fig. 13 gives the experimental setup and stress-strain curve with 0.2 % offset FYS and CYS strength for both tests.

Only the S9 sample suddenly broke with limited flexure right after crossing its elastic limit during bending. A tiny spring-back effect was observed in S3. All specimens performed a satisfactory FYS and CYS of more than 300 MPa. From Fig. 13 (a–b), S3 and S9 show the highest FYS of 452 MPa and the highest CYS of 539 MPa, respectively.

3.9. Wear resistance

An improvised wet sliding wear resistance test has been performed on an Ecomet 250 automatic grinder-polisher machine to identify the wear coefficient (K) of samples by using Archard's wear law [63] given in Eq. (2).

$$K = VH/WL \quad (2)$$

Where V is the wear volume, H is the hardness (Vickers), W is the applied load, and L is the sliding distance. Fig. 14 illustrates the testing setup. A customized reusable sample holder has been prepared to hold the sample firmly by mixing Epolam 2040 resin and Epolam 2042 hardener with a ratio of 100:33. The mold cavity is less than the sample thickness so that the sample surface can firmly attach with the abrasive paper. A total of 200 m distance has been traveled with a speed of 8.294 m/min, and data were recorded after 16.5 m (2 min), 50 m (6 min), 100 m (12 min), 150 m (24 min), 200 m (24 min) run. This experiment adopted an opposite directional (clockwise and counterclockwise) rotation (Fig. 14) to agitate the wear rate. The abrasive disk and sample holder were rotating at 30 rpm opposite each other, and a 10-pound force was applied to the samples. Running water (not placed directly on the testing sample) controlled the temperature and helped to remove debris from the site.

2000-grade polished samples were used to slide over silicon carbide abrasive papers, and the surface roughness of polished samples before the test was given in Table 4. The abrasive surface was eroded over time;

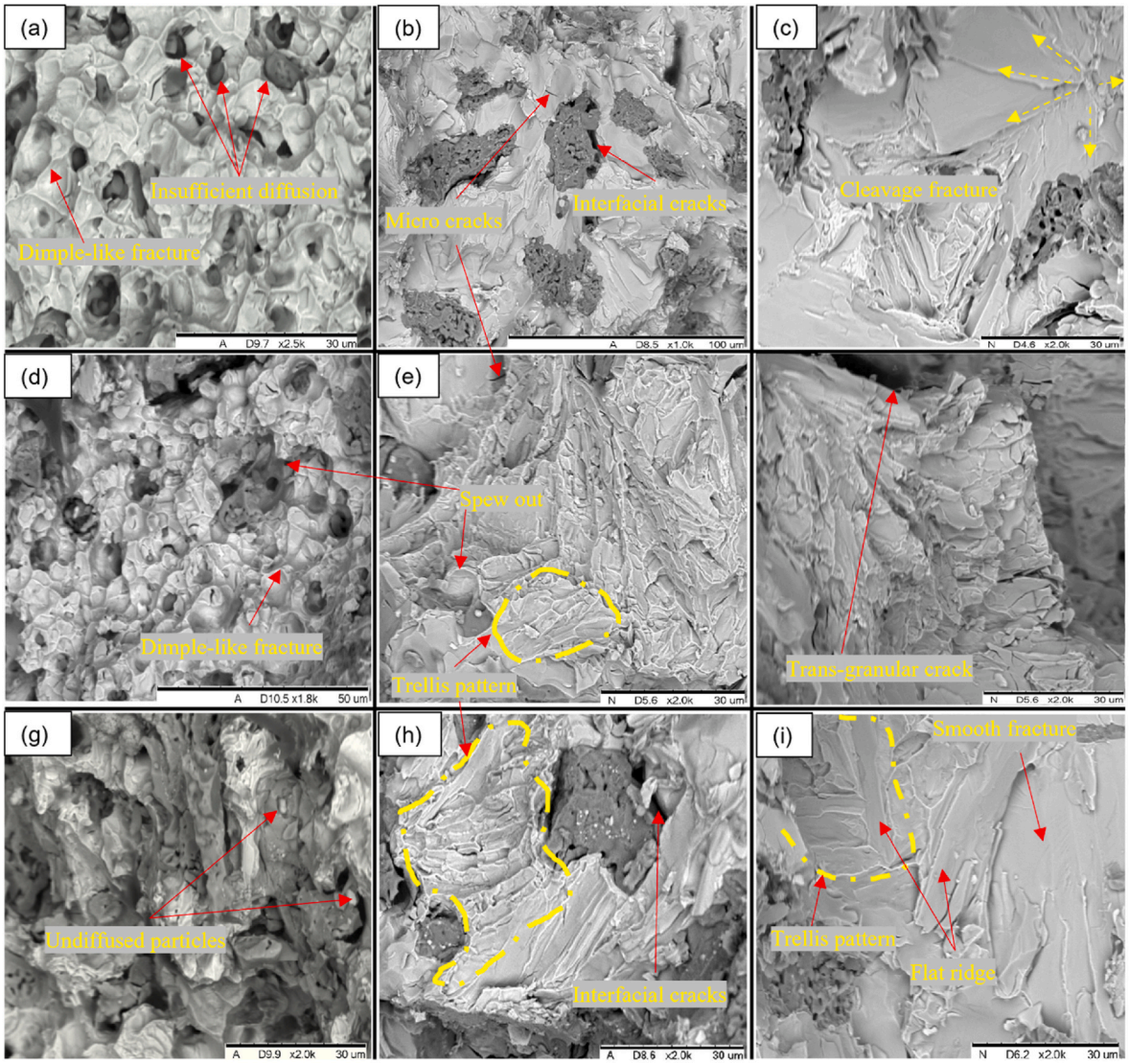

Fig. 11. SEM fractography of (a) S1, (b) S2, (c) S3, (d) S4, (e) S5, (f) S6, (g) S7, (h) S8, and (i) S9 after tensile test.

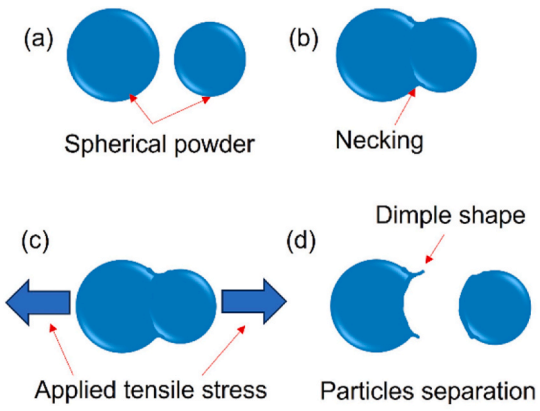

Fig. 12. The formation of a dimple-like structure during tensile test. Spherical particles become closer during sintering (a), forming weak necking (b). Applied tensile stress (c) breaks from the neck position and (d) leaves a dimple impression.

thence, it was changed every 2 min during the testing to maintain a comparable erosion effect to the new surface. The average roughness of the unused fresh abrasive surface was 3.54 μm, and after 2 min of rubbing, the average roughness dropped to 3.093 ± 0.142 μm (around 87.4 % abrasion ability). The surface roughness (Ra) and wear coefficient (K) of samples have been recorded before and after each testing stage and illustrated in Fig. 15.

Both the Ra and K values reduced with the increased sliding distance, followed by a plateau at the end. At the running-in stage, the two fresh surfaces came into contact and measured a higher Ra and K value after a 16.5 m pass. The continuous surface wear and mutual adaptation of the surface might be going to the steady-state condition. Also, the produced fine debris and water may form a tribofilm and work as a barrier to the abrasive surface-samples contact, reducing the wear coefficient to some extent and achieving wear coefficient stabilization [64]. Moreover, gradual wear with applied pressure can accomplish work hardening with few atoms thick from the exposed surface, thus reducing the wear coefficient. Nonetheless, no relation between the wear coefficient and surface roughness was observed. S8 showed the lowest roughness of 0.098 μm followed by S5 (0.103 μm) after the final pass. On the other hand, all the samples sintered at 1380 °C displayed a low K value. S6 surprisingly had significantly lower K (6.298×10^{-4}) than S9 (8.82×10^{-4}). In both cases, S1 underperformed by having Ra = 0.0186 μm and

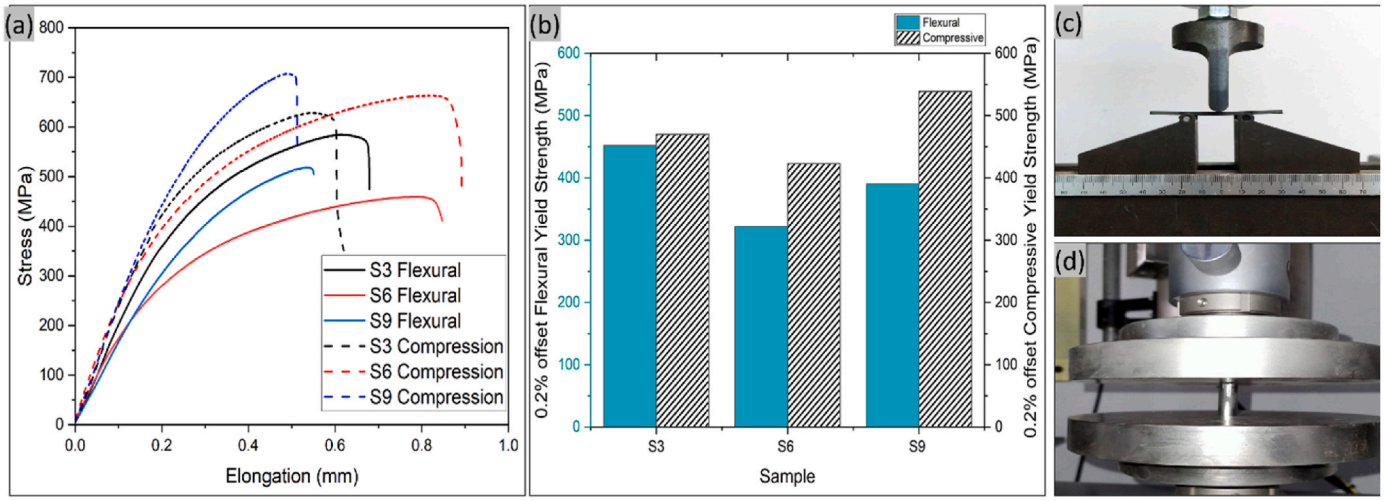

Fig. 13. Stress-strain curve for bending and compressive test of S3, S6, and S9 samples (a) with 0.2 % offset FYS and CYS (b). Testing set up for bending (c) and compression (d).

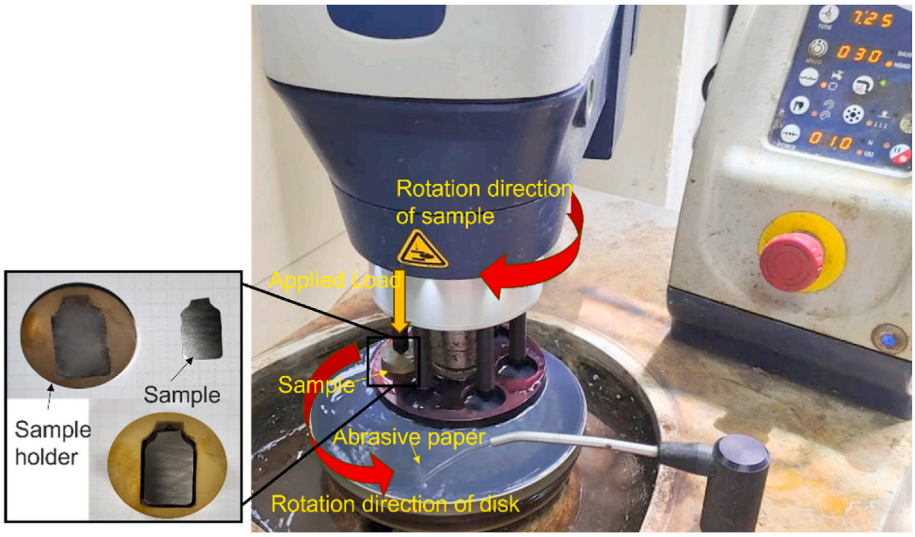

Fig. 14. Wear resistance test setup. Abrasive disk and sample mounting disk movement are opposite in direction. A removable sample holder (inset image) was used to mount and unmount samples easily.

Table 4
Surface roughness of polished samples.

Sample	S1	S2	S3	S4	S5	S6	S7	S8	S9
Ra (μm)	0.057	0.038	0.022	0.056	0.044	0.038	0.081	0.042	0.029

$K = 1.59 \times 10^{-3}$. Sintered temperature and Ti contents both have an impact on Ra and K. Sample sintered at higher temperature and high Ti content shows a relatively smoother surface profile due to the proper diffusion and presence of minimal pores. Similarly, a lower K value has been observed for high-temperature sintered samples. Diffused Ti in the matrix, depleted chromium carbides on the grain boundaries, and formation of intermetallic increase the hardness and suppress the wear tendency. Almost all the samples have shown a steady-state wear coefficient after a 150 m pass.

4. Conclusion

In this study, the physical and mechanical properties of Ti-reinforced 316L SS implant have been tested and can be summarized as follows.

1. Higher sintering temperature and Ti content increase the density. 5 vol% Ti sample sintered at 1300 °C achieved a densified part where 1 vol% and 3 vol% Ti samples produce porous parts at the same temperature, indicating an improved solid solubility due to the addition of Ti.
2. XRD analysis did not detect any TiC peak on any samples. Instead of the formation of TiC, carbon diffused within the matrix, thus reducing the formation of SiC and $Cr_{23}C_6$. Higher sintering temperatures and increased Ti contents help diffuse more Ti inside the matrix, forming Si_2Ti and Ti_3SiC_2, increasing the hardness and brittleness.
3. During the tensile test, materials mainly exhibited brittle fractures; however, some fractography showed a pseudo-dimple shape due to particle-particle separation caused by insufficient diffusion. Reduced

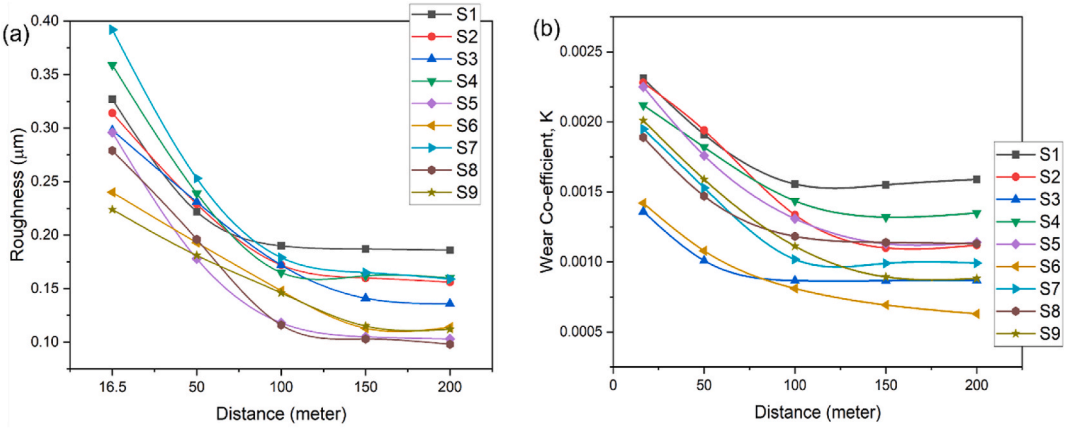

Fig. 15. Wear resistance test of 316L-SS samples. Distance vs surface roughness (a) and distance vs wear coefficient (b) indicate the wear behavior of samples.

modulus was obtained by increasing Ti and high sintering temperature. During the bending and compression test, S3 and brittle S9 samples outperformed S6 by achieving the highest 0.2 % offset FYS and CYS, respectively.

4. Sliding distance influences the wear coefficient, K, and surface roughness, Ra. Both the values were stable after a 150-m run, and S6 exhibited the highest wear resistance ability. Low-temperature sintered samples showed larger K and Ra values due to their inhomogeneous properties, although no correlation was found between them.

Declaration of competing interest

The authors declare that they have no known competing financial interests or personal relationships that could have appeared to influence the work reported in this paper.

Acknowledgment

Universiti Teknologi PETRONAS (UTP), Malaysia, provides funding support under Grant No. 015LC0-336. The authors acknowledge this gratefully.

References

[1] Methani MM, et al. Additive manufacturing in dentistry: current technologies, clinical applications, and limitations. Current Oral Health Reports 2020;7(4):327–34.
[2] Ahuja B, Karg M, Schmidt M. Additive manufacturing in production: challenges and opportunities. Laser 3d manufacturing II 2015;9353:11–20.
[3] Jang S, Park S, Bae C-j. Development of ceramic additive manufacturing: process and materials technology. Biomedical Engineering Letters 2020;10:493–503.
[4] Zhang H. Novel type of biomedical titanium-manganese-niobium alloy fabricated by arc melting and metal injection moulding. BTU Cottbus-Senftenberg; 2020.
[5] Ralls A, et al. Material design and surface engineering for bio-implants. J Miner Met Mater Soc 2020;72:684–96.
[6] Kurup A, Dhatrak P, Khasnis N. Surface modification techniques of titanium and titanium alloys for biomedical dental applications: a review. Mater Today Proc 2021;39:84–90.
[7] Kabir S, et al. Review of the developments in composite materials over the last 15 years. 2023.
[8] Walunj G, et al. Light weight-low modulus biocompatible titanium alloys processed via spark plasma sintering. Journal of Alloys and Metallurgical Systems 2023:100018.
[9] Nakai M, et al. Concept and fabrication of beta-type titanium alloy rod with parts possessing different Young's moduli for spinal fixation. Mater Trans 2023;64(1):147–54.
[10] Romero-Resendiz L, et al. Development of a porous Ti–35Nb–5In alloy with low elastic modulus for biomedical implants. J Mater Res Technol 2023;22:1151–64.
[11] Šípová M, et al. A study on the corrosion behaviour of stainless steel 08Cr18Ni10Ti in supercritical water 2023;211:110853.
[12] Dwivedi S, Rai Dixit A, Kumar Das A. Wetting behavior of selective laser melted (SLM) bio-medical grade stainless steel 316L. Mater Today Proc 2022;56:46–50.
[13] Lodhi MK, et al. Additively manufactured 316L stainless steel with improved corrosion resistance and biological response for biomedical applications 2019;27:8–19.
[14] Saravanan M, et al. A review on recent progress in coatings on AISI austenitic stainless steel. Mater Today Proc 2018;5(6):14392–6.
[15] Malhotra D, Dhillon JS, Shahi A. New insights into metallurgical, corrosion, passive film and fatigue characteristics of AISI 316L submerged arc welded joints. J Mater Sci 2022;57(41):19571–91.
[16] Pardo A, et al. Influence of Ti, C and N concentration on the intergranular corrosion behaviour of AISI 316Ti and 321 stainless steels 2007;55(7):2239–51.
[17] Kasana SS, Pandey O. Effect of heat treatment on microstructure and mechanical properties of boron containing Ti-Stabilized AISI-321 steel for nuclear power plant application. Mater Today Commun 2021;26:101959.
[18] Bocchetta P, et al. Passive layers and corrosion resistance of biomedical Ti-6Al-4V and β-Ti alloys 2021;11(5):487.
[19] Hanawa T. Biocompatibility of titanium from the viewpoint of its surface. Sci Technol Adv Mater 2022;23(1):457–72.
[20] Hanawa T, Ota M. Calcium phosphate naturally formed on titanium in electrolyte solution. Biomaterials 1991;12(8):767–74.
[21] Rodchenkov B, et al. Irradiation behavior of Ti-stabilized 316L type steel 2009;386:277–80.
[22] Loto RT. Corrosion resistance and morphological deterioration of 316Ti austenitic, GX4CrNiMo16-5-1 martensitic and 444 ferritic stainless steels in aqueous corrosive environments 2019;14:102423.
[23] Zhai W, Zhou W, Nai SML. Grain refinement of 316L stainless steel through in-situ alloying with Ti in additive manufacturing. Mater Sci Eng 2022;840:142912.
[24] Mieloch AA, et al. Osteoarthritis severely decreases the elasticity and hardness of knee joint cartilage: a nanoindentation study. J Clin Med 2019;8(11):1865.
[25] Dempster WT, Coleman RF. Tensile strength of bone along and across the grain. J Appl Physiol 1961;16(2):355–60.
[26] Hallab NJ, Jacobs JJ. Orthopedic applications. In: Biomaterials science. Elsevier; 2020. p. 1079–118.
[27] Attar H, et al. Mechanical behavior of porous commercially pure Ti and Ti–TiB composite materials manufactured by selective laser melting. Mater Sci Eng 2015;625:350–6.
[28] Jin W, Chu PK. Orthopedic implants. Encyclopedia of biomedical engineering 2019;1(3):425–39.
[29] Cunningham C, et al. Effects of in-process LN2 cooling on the microstructure and mechanical properties of type 316L stainless steel produced by wire arc directed energy deposition. Mater Lett 2021;282:128707.
[30] Shahed CA, et al. Antibacterial mechanism with consequent cytotoxicity of different reinforcements in biodegradable magnesium and zinc alloys: a review. J Magnesium Alloys 2023;11(9):3038–58.
[31] Sas A, et al. Effect of anatomical variability on stress-shielding induced by short calcar-guided stems: automated finite element analysis of 90 femora 2019;37(3):681–8.
[32] Yılmaz E, et al. Metallurgical properties and biomimetic HA deposition performance of Ti-Nb PIM alloys 2018;746:301–13.
[33] Chen J-H, et al. Boning up on Wolff's Law: mechanical regulation of the cells that make and maintain bone 2010;43(1):108–18.
[34] Qin R, et al. Effect of sintering temperature on microstructure characteristics and damping capacity of multilayer 316L stainless steel hollow spheres/A356 alloy composites reinforced by NiTi alloy sheets. Mater Sci Eng 2022;860:144321.
[35] Hwang I-S, et al. Characterization of mechanical properties and grain size of stainless steel 316L via metal powder injection molding. Materials 2023;16(6):2144.
[36] Shieddieque AD, et al. Effects of sintering variables on the physical and mechanical properties of metal injection molding molded 17-4 ph stainless steel. In: Materials science forum. Trans Tech Publ; 2021.
[37] Xianfeng Y, et al. Study of thermal degradation mechanism of binders for ceramic injection molding by TGA-FTIR. Ceram Int 2019;45(8):10707–17.

[38] Li Q, et al. Comparison of laser-clad and furnace-melted Ni-based alloy microstructures. Surf Coating Technol 2001;137(2–3):122–35.
[39] Sun L, et al. First principles investigation of binary chromium carbides Cr7C3, Cr3C2 and Cr23C6: electronic structures, mechanical properties and thermodynamic properties under pressure. Materials 2022;15(2):558.
[40] Liu S, et al. Growth characteristics of primary M7C3 carbide in hypereutectic Fe-Cr-C alloy. Sci Rep 2016;6(1):32941.
[41] Ahmed N, et al. Si diffusion induced adhesion and corrosion resistance in annealed RF sputtered SiC films on graphite substrate. Ceram Int 2022;48(8):11009–17.
[42] Córdoba JM, et al. Synthesis of Ti3SiC2 powders: reaction mechanism. J Am Ceram Soc 2007;90(3):825–30.
[43] Kherrouba N, et al. Experimental study and simulation of the σ phase precipitation in the stabilized 316Ti austenitic stainless steel. Mater Chem Phys 2021;266:124574.
[44] Deng P, et al. Evolution and impact of oxygen inclusions in 316L stainless steel manufactured by laser powder bed fusion. Thermomechanics & infrared imaging, inverse problem methodologies and mechanics of additive & advanced manufactured materials, vol. 7. Cham: Springer International Publishing; 2021.
[45] Schmuecker SM, et al. Synthesis of metastable chromium carbide nanomaterials and their electrocatalytic activity for the hydrogen evolution reaction. Dalton Trans 2017;46(39):13524–30.
[46] Jiang C. First-principles study of structural, elastic, and electronic properties of chromium carbides. Appl Phys Lett 2008;92(4):041909.
[47] Sun L, et al. Interface characterization and mechanical properties of Mo-added chromium carbide-nickel composite. Ceram Int 2020;46(17):27071–9.
[48] Momeni V, et al. Investigating the effect of stearic acid on the mechanical, rheological, and microstructural properties of AISI 4605 feedstock for metal injection molding process. Trans Indian Inst Met 2021;74(9):2161–70.
[49] Yoshikawa T, et al. Thermodynamics of impurity elements in solid silicon. J Alloys Compd 2010;490(1–2):31–41.
[50] Di Pierro S, et al. Rock-forming moissanite (natural α-silicon carbide). Am Mineral 2003;88(11–12):1817–21.
[51] Chou TC, Joshi A. Selectivity of silicon carbide/stainless steel solid-state reactions and discontinuous decomposition of silicon carbide. J Am Ceram Soc 1991;74(6):1364–72.
[52] Yeh C, Chen W, Hsu C. Formation of titanium silicides Ti5Si3 and TiSi2 by self-propagating combustion synthesis. J Alloys Compd 2007;432(1–2):90–5.
[53] Tabares E, Jiménez-Morales A, Tsipas SA. Study of the synthesis of MAX phase Ti3SiC2 powders by pressureless sintering. Bol Soc Espanola Ceram Vidr 2021;60(1):41–52.
[54] Kolli RP, Devaraj A. A review of metastable beta titanium alloys. Metals 2018;8(7):506.
[55] Zhang H, et al. Novel type of biomedical titanium-manganese-niobium alloy fabricated by metal injection moulding. In: Euro PM congress & exhibition; 2019.
[56] Carminati M, et al. Mechanical characterization of AISI 316L samples printed using material extrusion. Appl Sci 2022;12. https://doi.org/10.3390/app12031433.
[57] Tromas C, et al. Hardness and elastic modulus gradients in plasma-nitrided 316L polycrystalline stainless steel investigated by nanoindentation tomography. Acta Mater 2012;60(5):1965–73.
[58] Musil J, et al. Relationships between hardness, Young's modulus and elastic recovery in hard nanocomposite coatings. Surf Coating Technol 2002;154(2):304–13.
[59] Hafeez N, et al. Superelastic response of low-modulus porous beta-type Ti-35Nb-2Ta-3Zr alloy fabricated by laser powder bed fusion. Addit Manuf 2020;34:101264.
[60] Bender S, et al. Mechanical characterization and modeling of graded porous stainless steel specimens for possible bone implant applications. Int J Eng Sci 2012;53:67–73.
[61] Rehmer B, et al. Elastic modulus data for additively and conventionally manufactured variants of Ti-6Al-4V, IN718 and AISI 316 L. Sci Data 2023;10(1):474.
[62] Maity T, et al. High pressure torsion induced lowering of Young's modulus in high strength TNZT alloy for bio-implant applications. J Mech Behav Biomed Mater 2020;108:103839.
[63] Archard J. Contact and rubbing of flat surfaces. J Appl Phys 1953;24(8):981–8.
[64] Yang X, et al. Effects of tribo-film on wear resistance of additive manufactured cobalt-based alloys during the sliding process. Surf Coating Technol 2021;427:127784.